3-1-2023

Wetting hysteresis as the mechanism of heat pipe post-dryout thermal hysteresis and recovery

K. Baraya

Justin Weibel
jaweibel@purdue.edu

S. V. Garimella

Baraya, K.; Weibel, Justin; and Garimella, S. V., "Wetting hysteresis as the mechanism of heat pipe post-dryout thermal hysteresis and recovery" (2023). *CTRC Research Publications.* Paper 403.
http://dx.doi.org/https://doi.org/10.1016/j.ijheatmasstransfer.2023.123875

Wetting Hysteresis as the Mechanism of Heat Pipe Post-Dryout Thermal Hysteresis and Recovery

Kalind Baraya, Justin A. Weibel[1], Suresh V. Garimella[2]
School of Mechanical Engineering
Purdue University, 585 Purdue Mall, West Lafayette, IN 47907 USA

Abstract

Heat pipes and vapor chambers are passive thermal management devices used for efficient heat transport by phase change. Their passive operation is enabled by capillary pumping of the working fluid in a porous wick, which is operationally limited by the maximum pressure head it can provide. This capillary limit marks the maximum heat input at which the capillary pressure generated can overcome the pressure drop in the wick; operating above the capillary limit at steady state leads to dryout. Heat pipes and vapor chambers are increasingly being used in electronics systems where end-user activity dictates the transient power input which can therefore be highly variable and time-dependent. It was recently shown that heat pipes can withstand a power pulse exceeding the capillary limit for brief time intervals. Under such operating conditions, the heat pipe will experience dryout only if the duration of the pulse load is longer than a certain characteristic time interval. The pulse-load-induced dryout may result in an increased thermal resistance when the power is reduced back down to pre-dryout levels, thus exhibiting a hysteresis in heat pipe thermal performance. In this work, we experimentally characterize the recovery from pulsed-load-induced dryout. We further propose that the observed change in steady-state thermal performance before and after dryout results from contact angle hysteresis at the three-phase contact line of the wick-liquid interface. A model is developed based on this proposed mechanism to predict the nature of recovery from dryout-induced thermal hysteresis, as well as to identify that a given heat pipe has a maximum possible hysteresis. The experiments illustrate the trends inferred from the model for the recovery process and confirm the existence of a "maximum hysteresis line," which identifies the worst-case scenario for thermal hysteresis after heat pipe dryout. Based on these mechanistic learnings, a new testing protocol is proposed for experimentally characterizing this post-dryout maximum hysteresis signature for a heat pipe.

Keywords: heat pipe, vapor chamber, capillary limit, dryout, recovery, hysteresis

[1] Corresponding author, E-mail address: jaweibel@purdue.edu.
[2] Currently President, University of Vermont

Nomenclature

ΔP_{wick}	Total wick pressure drop (Pa)	x, y, z	Coordinate axis (m)
h	Heat transfer coefficient (W m^{-2} K^{-1})	W	Width (m)
h_{fg}	Latent heat of vaporization (J kg^{-1})		
h_{vap}	Vapor core thickness (m)	***Subscripts***	
h_{wall}	Wall thickness (m)	A	Evaporator region with saturated wick
h_{wick}	Wick thickness (m)	A′	Evaporator region with dry wick
k	Wall thermal conductivity (W m^{-1} K^{-1})	B	Condenser region with saturated wick
K	Wick permeability (m^2)	B′	Condenser region with dry wick
L_a	Adiabatic length (m)	l	Liquid
L_c	Condenser length (m)	sat	Saturated
l_{dry}	Dryout length (m)	evap	Evaporator
L_e	Evaporator length (m)	cond	Condenser
L_{hp}	Heat pipe length (m)	wick	Wick
m''	Mass flux in evaporator region (kg m^{-2})	v	Vapor
P	Pressure (Pa)		
$P_{o,sat}$	Reference saturation pressure (Pa)	***Greek***	
$P_{c,max}$	Maximum capillary pressure (Pa)	μ	Fluid viscosity (N s m^{-2})
$\bar{P}$	z-averaged pressure (Pa)	ρ	Fluid density (kg m^{-3})
q''	Heat flux (W m^{-2})	θ	Interface contact angle (rad)
R_g	Gas constant (J kg^{-1} K^{-1})	σ	Accommodation coefficient (-)
T	Temperature (K)	θ_r	Receding contact angle (rad)
t_{hp}	Heat pipe thickness (m)	θ_a	Advancing contact angle (rad)
$T_{o,sat}$	Reference saturation temperature (K)	β	l_{dry}/L_{hp} (-)
T_∞	Ambient temperature (K)	ϕ	$\frac{2\sigma}{2-\sigma}\frac{h_{fg}\rho_v}{T_{sat}^{1.5}}\left(\frac{1}{2\pi R}\right)^{0.5}$ (kg m^{-2} s^{-1} K^{-1})
u	Velocity (m s^{-1})		

1. Introduction

Heat pipes and vapor chambers are liquid-vapor phase-change devices used for hotspot mitigation and efficient heat transfer in electronics and other systems [1, 2]. These devices consist of a hermetically sealed metallic casing lined on the inside with a porous wick that is saturated with working liquid [3]. The porous structure provides surface area for fluid evaporation at the region of a heat source, and its capillary action

facilitates passive operation of the device. The vapor generated near the heat source flows to the condenser end where heat is rejected; the condensate is passively pumped back to the heat input region due to the capillary pressure generated in the microscale pores of the wick. The pressure drop in the wick is thus governed by the heat input (and corresponding flow rate of vapor/condensate) and is supported by the capillary pressure head. A maximum heat input called the capillary limit exists at which the pressure drop across the wick and the vapor core is balanced by the maximum capillary pressure head that the wick can provide [3]. Operating a heat pipe above the capillary limit at steady state is accompanied by dryout at the heat input region and a significant increase in thermal resistance.

Most experimental studies in the literature have focused on characterizing steady-state heat pipe performance in terms of thermal resistance. Heat transfer mechanisms and thermal performance of wicks have been characterized under conditions that simulate heat pipe operation. Iverson et al. [4] measured the evaporation rate from a heated porous sample into a saturated vapor environment and showed that a majority of the heat transfer occurs through evaporation from the porous medium as opposed to thermal conduction along the length of the wick. Liou et al. [5] characterized the performance of screen-mesh wicks, for which the thermal resistance was found to decrease with an increase in heat input. They reasoned that the decrease in thermal resistance was due to recession of liquid level in the wick as the heat input increased. Similar observations of a decrease in thermal resistance with increasing power input were made by Wong et al. [6] for sintered copper powder wicks. Apart from characterizing the influence of the wick on heat pipe performance, several researchers have experimentally studied the effects of other operational and geometric factors on heat pipe performance. For example, surface wettability of the wick material was found to affect only the capillary limit, with no other significant effect on the thermal performance [7]. In another study, Kempers et al. [8] showed that the thermal resistance of a heat pipe generally increases with increase in the amount of liquid charge in the wick. Oversaturated wicks in particular, in which the amount of liquid exceeded the available pore space in the wick, led to a significantly higher thermal resistance due to liquid pooling in the heat pipe condenser region. Chang et al. [9] conducted experiments to show that a spatially non-uniform heat flux had no impact on the thermal resistance of a flat heat pipe.

In addition to these experimental studies, numerous investigations have also used numerical and analytical models to characterize and predict the steady-state heat pipe thermal resistance. Prasher et al. [10] developed a reduced-order thermal resistance network approach to predict vapor chamber and heat pipe thermal resistance using an effective thermal conductivity for transport though the vapor core. This modeling approach was later used by Sauciuc et al. [11] to benchmark vapor chamber thermal performance against metal heat spreaders. A design envelope was identified in which vapor chambers offer lower thermal resistance than metal spreaders below a threshold spreader thickness. The choice of working fluid has also

been shown to have a considerable effect on the heat pipe thermal resistance. Using a thermal resistance network model, Yadavalli et al. [12] explored the design space of ultra-thin heat-pipe form factors and identified the resistance imposed by the vapor pressure drop as an important additional factor affecting performance; at these ultra-thin form factors, the heat pipe must exceed a minimum thickness to offer lower thermal resistance than a metal spreader. A vapor figure-of-merit was defined in terms of the vapor thermophysical properties, and fluids with higher vapor figure-of-merit were shown to reduce this minimum thickness threshold. Recently, a more holistic approach of choosing both the working fluid and the wick in conjunction was offered for designing heat pipes with minimized thermal resistance [13].

The studies reviewed above characterize the performance of a heat pipe under steady-state operation. However, heat pipes and vapor chambers are used in applications where the nature of the heat load can be highly dynamic [14–17]. This has motivated a characterization of the transient performance of heat pipes using computational and experimental methods. Early work by Tournier and El-Genk [18] on modeling the transient response of a heat pipe accounted for excess liquid pooling in the condenser region. The model was used to predict heat pipe thermal response during startup and shutdown processes and showed good agreement with experiments. Modeling efforts have also been used to benchmark the transient response of a heat pipe or vapor chamber to a solid heat spreader, and the temperature rise in a solid spreader was shown to be slower than a heat pipe or vapor chamber during short-interval thermal cycles [19]. Transient models have also been utilized to study the effect of multiple discrete sources on the thermal response of a heat pipe or vapor chamber, which led to the conclusion that the effect of spreading in the wick and the wall cannot be neglected [20]. Recent studies have sought to identify the mechanisms that govern transient transport in a heat pipe or vapor chamber using experimentally validated semi-analytical models for heat pipe transport [21].

The studies reviewed to this point have investigated the governing transport mechanisms and characterized heat pipe thermal performance for both steady-state and transient operations *up to* the capillary limit. Heat pipes and vapor chambers are typically sized to have a capillary limit that is near or above the thermal design power (TDP) [22] that represents a time-averaged heat input from an electronic device. However, vapor chambers and heat pipes are increasingly finding uses in applications having highly transient heat inputs where heat input may exceed this steady-state TDP [22], and often also the capillary limit. While device operation above the TDP may last for a brief time interval [23], operating the heat pipe above the capillary limit poses a risk for dryout that is critical to understand and assess. Our previous work [24] has shown that the heat pipe undergoes dryout if operated above the capillary limit for a time interval exceeding a characteristic time called time-to-dryout. The occurrence of dryout during such pulse-load operation above the capillary limit makes the heat pipe susceptible to performance degradation, specifically thermal

hysteresis after the power level drops back to below the capillary limit. Moreover, the heat pipe was unable to recover its pre-dryout thermal performance unless the heat input was lowered to a value significantly lower than the capillary limit. Hence, there is a critical need to characterize heat pipe thermal hysteresis and recovery *post-dryout*.

In this work, we propose that the contact angle hysteresis observed at the liquid-vapor-wick interface in a heat pipe governs the dryout-induced thermal hysteresis. A model that accounts for this wetting hysteresis mechanism is developed to predict the nature of thermal recovery of a heat pipe after dryout. Using the model, it is shown that the thermal resistance as function of power for a given heat pipe recovering from dryout has a worst-case scenario which is represented by a *maximum hysteresis* line. This maximum hysteresis line is found to be independent of the history of the dryout-inducing pulse load. Experiments are performed to confirm the existence of this maximum hysteresis line in a heat pipe during recovery from dryout. Lessons from this work are employed to propose a new experimental paradigm for characterizing the dryout and recovery behavior of heat pipes.

2. Experimental setup

A schematic diagram of the experimental testing configuration for the heat pipes is shown in Figure 1. This setup is similar to the one described in detail in our previous work [24] and is only briefly introduced here. A heat pipe sample is balanced on top of polystyrene supports on both ends to minimize the introduction of additional thermal capacity during transient testing. The data presented in the following sections are obtained using two commercial copper-water heat pipe (Novark Technologies) of identical length (L_{hp} =130 mm) and width (W = 8.6 mm), but with different thicknesses (t_{hp} = 0.87 mm and 0.62 mm). The heat pipes have a resistive heater (nichrome wire sheathed in polyimide) wound on one end to form the evaporator section, and the remaining surface is used as the condenser for rejecting heat to the ambient using forced convection. An adjustable convection shield allows for the length of the condenser section to be controlled. A T-type thermocouple is sandwiched between the heater sheath and the heat pipe surface to measure the evaporator temperature. All thermocouples have a manufacturer-specified uncertainty of ±0.3 °C and are referenced to an ice point (OMEGA TRCIII) temperature maintained at 0 °C as monitored by an RTD. The ambient air temperature is also monitored by an RTD.

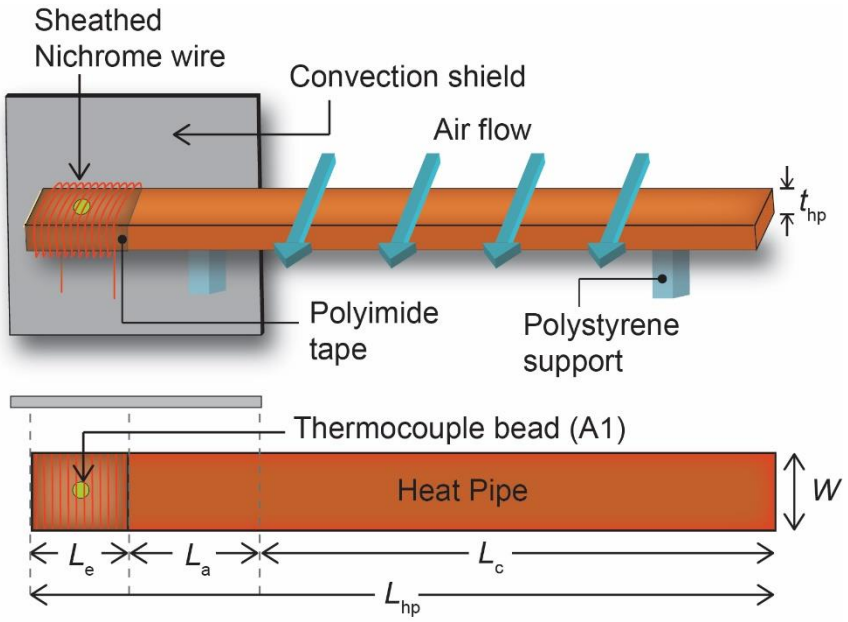

Figure 1. Schematic diagram of the experimental setup. The heat pipe is supported on narrow polystyrene supports and features a resistive heater of length L_e = 10 mm on one end. The remaining condenser surface is cooled by forced convection. A thermocouple is used to measure temperatures at the evaporator (A1). Two heat pipe samples are used for this study having the same length (L_{hp}) of 130 mm and width (W) of 8.6 mm, while having differing in total thickness (t_{hp}) of 0.87 mm and 0.62 mm.

A programmable power source (Koard KA3005P) powers the heater. A National Instruments (NI) cDAQ-9178 chassis is used to acquire the experimental measurements. The chassis is equipped with modules for thermocouple measurements (NI-9214), RTD measurement (NI-9217), and for measuring the voltage drop across the heater (NI-9205). In Ref. [24], the heat loss from the heater was calibrated over a range of 1 W to 7 W and found to be within 5% to 9% of the total supplied power input. The experimental power inputs reported in the following sections refer to the supplied power before accounting for this heat loss. The thermal resistance of the heat pipe is defined based on the supplied power and the temperature differential between the evaporator temperature (location A1 in Figure 1) and the ambient temperature.

3. Mechanism of heat pipe thermal hysteresis after dryout

As reviewed above, our previous work confirmed that heat pipes exhibit thermal hysteresis in performance after the occurrence of dryout, even when the power input drops below the capillary limit [24]. In the current work focusing on the mechanism of thermal hysteresis, the heat pipe sample (L_{hp} = 130 mm, W = 8.6 mm, t_{hp} = 0.62 mm) thermal resistance is characterized under two stages of operation that differ in their initial

heat input to the heat pipe: 1) in the *powering-up* stage, the heat pipe starts from zero heat input and the power is increased to beyond the capillary limit; and 2) in the *powering-down* stage, the heat pipe starts from a power that induced capillary dryout of the evaporator which is then reduced back to zero in steps.

During the powering-up stage, the heat input to the heat pipe is increased from 0 W in finite increments that become finer as the capillary limit is approached. At each heat input level, the heat pipe is allowed to reach steady state and the corresponding thermal resistance is recorded. Figure 2(a) plots the thermal resistance with power for both stages, with the powering-up stage shown in darker gray. The solid symbols are the experimentally measured data points connected by dashed line segments, while the thicker solid line overlaid on the solid symbols calls attention to the overall trend. It can be observed that the heat pipe thermal resistance with respect to the ambient temperature (23 °C) gradually decreases with heat input until the increment above 5.1 W causes a steep increase in the thermal resistance. This significant increase in the thermal resistance indicates that a dryout has occurred at the evaporator, and therefore 5.1 W is deduced to be the capillary limit of the heat pipe.

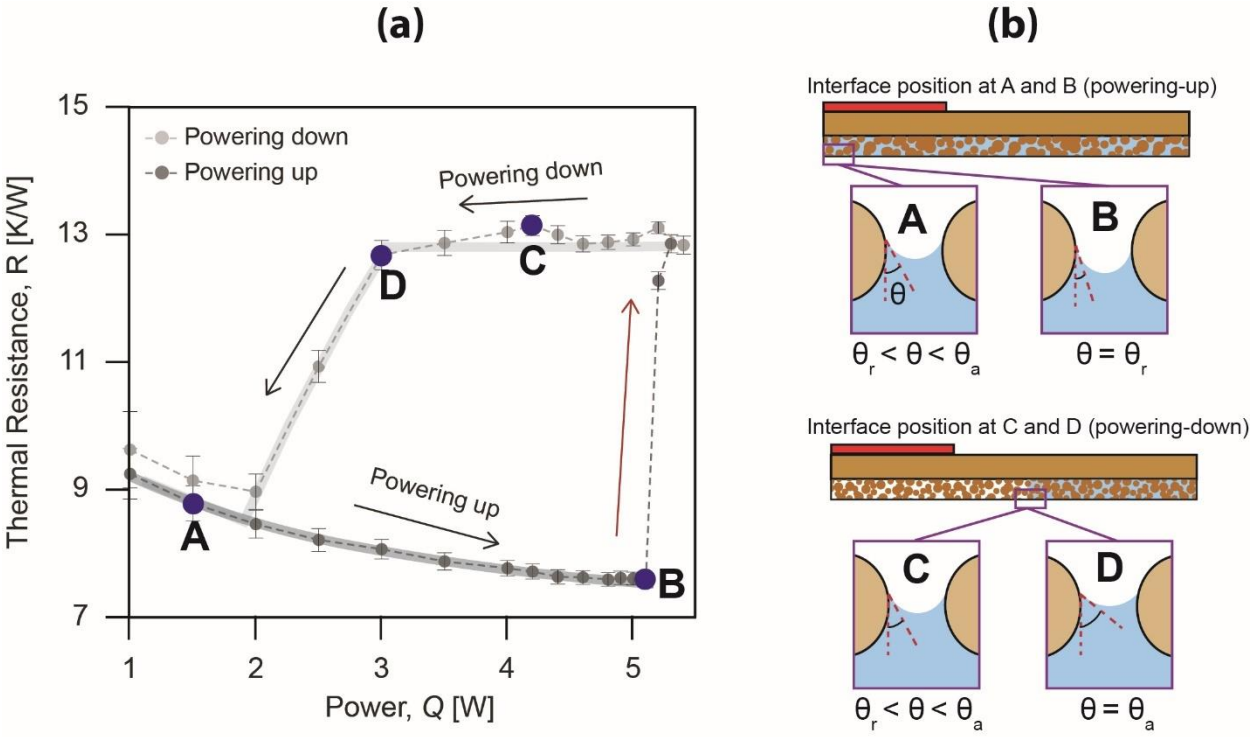

Figure 2. Thermal hysteresis in a heat pipe after dryout. (a) Thermal resistance of the heat pipe measured during powering-up beyond the capillary limit and powering-down after dryout has occurred. (b) Schematic

representation of the contact angle at the wick-vapor core interface for the four positions marked A, B, C, and D on the thermal resistance plot.

After the occurrence of dryout, the heat input is lowered in finite decrements in the powering-down stage. At each heat input during this stage, the heat pipe is allowed to reach a steady state before the thermal resistance is measured, as plotted in Figure 2(a) in lighter gray. Several key observations can be made from the heat pipe thermal response during this powering down stage. Over a broad range of heat inputs below the capillary limit, the thermal resistance during powering down is significantly higher than the values during powering up. This difference between the thermal resistances during the powering-up and powering-down stages is the significant thermal hysteresis that is induced in the heat pipe by the dryout event. Specifically, as the heat input begins to decrease during the powering-down stage, the thermal resistance remains practically unchanged from the high value attained after the dryout event. Only when the heat input falls below 3 W does the resistance begins to decrease and the difference between the powering-down and powering-up curves diminishes. The difference nearly vanishes at the input of 2 W, where the powering-down curve essentially merges with the powering-up curve (the slight remaining difference is within the measurement uncertainty).

This post-dryout thermal hysteresis observed in the heat pipe is attributed to capillary hysteresis in the flow in the porous wick of the heat pipe. Hydrodynamic or capillary pressure hysteresis in porous structures is a well-known phenomenon that has been extensively observed in other contexts. The observed hysteresis has been attributed to several different mechanisms, the most common of which are the spatial variation of pore size, liquid pockets formation due to disconnected liquid domains, and wetting hysteresis [25]. Of these, liquid pocket formation due to disconnected domains can be ruled out as a significant cause of hysteresis because the porous structure in the current study is a heat pipe wick that is in a so-called “over-dry” situation. Because the wick is heated at the evaporator, any isolated liquid pockets would eventually completely evaporate due to heating in the absence of any influx of replenishing liquid. Spatial variation of pore size can indeed be a significant contributor to capillary hysteresis, and thereby to the thermal hysteresis observed in the heat pipe. However, if pore size variation were a major contributor to capillary hysteresis, then the trends of thermal hysteresis as observed in the experiments would be sample-specific, and the trends would not hold true for other heat pipe samples with different wick types and geometry. As will be shown in the following discussions (Section 5.1 and Appendix A), we observe that a characteristic trend in thermal hysteresis behavior is observed across various heat pipe samples with different wick types and geometry.

We thus postulate that the observed thermal hysteresis after dryout is primarily due to the contact angle hysteresis occurring at the liquid-vapor-wick three-phase contact lines in the evaporator region, where the

local contact angle and meniscus curvature are determined by the capillary pressure. To briefly review these wetting phenomena, contact angle hysteresis is the difference between the advancing and the receding contact angles at a three-phase contact line. The advancing contact angle is the angle at which the three-phase contact line begins to advance (i.e., wet the solid phase), while the receding contact angle is the angle at which the contact line starts to recede (i.e., de-wet). In the context of a heat pipe, interface recession is defined as the non-wetting vapor phase displacing the wetting liquid phase in the copper wick, while advancing is defined as wetting liquid phase displacing the non-wetting vapor phase in the wick. Wetting hysteresis always exists to some degree, and many practical surface-fluid combinations exhibit significant contact angle hysteresis due to the presence of surface roughness and chemical heterogeneity. It should be noted that the advancing and the receding contact angles, and thereby contact angle hysteresis, are specific to a given surface-fluid combination and morphology. For water-copper surfaces (smooth and oxide-free), it has been extensively shown in the literature that significant contact angle hysteresis exists [24–26], implying that the advancing contact angle is much higher than the receding contact angle. Bonn et al. [29] provided a detailed review of the physics governing contact line dynamics and contact angle hysteresis at the three-phase contact line.

The schematic of heat pipe cross section in Figure 2(b) includes a zoomed-in view of the microscopic wick-vapor interface showing the three-phase contact line. During the powering-up stage at heat loads lower than the capillary limit, marked as point A on the powering-up curve (Figure 2(a)), the heat pipe wick is saturated at the evaporator. The contact angle, θ, is higher than the receding contact angle (θ_r), as shown by the contact line at point A. As the heat load increases, the pressure head generated in the wick must increase commensurately, thus leading to an increase in the meniscus curvature and reduction in the contact angle. Specifically, the capillary pressure head provided by the wick is proportional to the cosine of the contact angle, which determines the degree of contact angle decrease with an increase in input power. At the capillary limit, marked as point B, the contact angle reaches the receding contact angle. Any finite increase in heat input above this limit leads to dryout, and a dry patch is formed over the evaporator region due to interface recession. As the interface can only recede at the receding contact angle, the contact angle at the capillary limit must be the receding contact angle.

After dryout has occurred, the interface has receded to a new position where the contact angle is governed by the pressure drop in the wick and exceeds the receding contact angle. During the powering-down stage post-dryout, the pressure drop in the heat pipe decreases as the heat input is decreased. Consequently, the interface contact angle increases in response to the pressure drop change. However, below the capillary limit, within the range where the thermal resistance is constant as denoted by point C on the powering-down curve, the contact angle is still less than the advancing contact angle (θ_a). Even though the pressure

drop in the wick decreases, the interface cannot advance because the contact angle is yet to reach the advancing contact angle. Hence, the interface remains pinned at the dryout location, thus explaining the unchanged thermal resistance with decrease in heat input. At point D, the contact angle has just reached the advancing contact angle, and the interface will advance with any further finite decrease in power, thus leading to a decrease in thermal resistance as well. Ultimately, at 2 W, the interface fully rewets the evaporator region and thus the thermal hysteresis is fully reversed.

4. Mechanistic model development

An analytical model is developed to predict heat pipe thermal resistance during these powering-up and powering-down stages based on the hypothesis that the thermal hysteresis is caused by wetting hysteresis. The model solves for the thermal resistance at steady state by balancing the wick pressure drop with the maximum capillary pressure head that the wick can provide. The inputs to the model are the wick properties (effective pore radii, permeability); wick, wall, and vapor core thickness; working fluid properties (evaluated at the vapor core saturation temperature); and advancing and receding contact angles for the fluid-substrate combination. This section describes the model setup, key model assumption, and solution procedure.

The setup for the model is shown in Figure 3, where the objective is to replicate the heat pipe boundary conditions and geometry used in the experiments (Figure 1). Case I in Figure 3 shows a complete cross-section of the flat heat pipe geometry under consideration (the remaining cases show a simplified view of only the lower half of the geometry). At one end of the heat pipe is the evaporator, and the remaining surface is the condenser. Case I represents the heat pipe operation before dryout at heat inputs lower than the capillary limit. For modeling purposes, the heat pipe is divided into two zones along the length, such that Zone A is the evaporator region and Zone B is the condenser region. Mass, energy, and momentum transfer are solved for separately in each zone, and the zones are coupled using suitable boundary conditions. Case II represents the heat pipe under conditions where the evaporator experiences partial dryout, that is, the dryout front is in the evaporator region of the wick. For Case II, the domain is divided into three zones: the evaporator region with dryout (Zone A′), the evaporator region where the wick remains saturated (Zone A), and the condenser region (Zone B). Case III represents the heat pipe operation when the evaporator is completely dried out and the interface has receded into the condenser region. Case III is divided into zones for the evaporator with complete dryout (Zone A′), the condenser region under dryout (Zone B′), and the condenser region with saturated wick (Zone B).

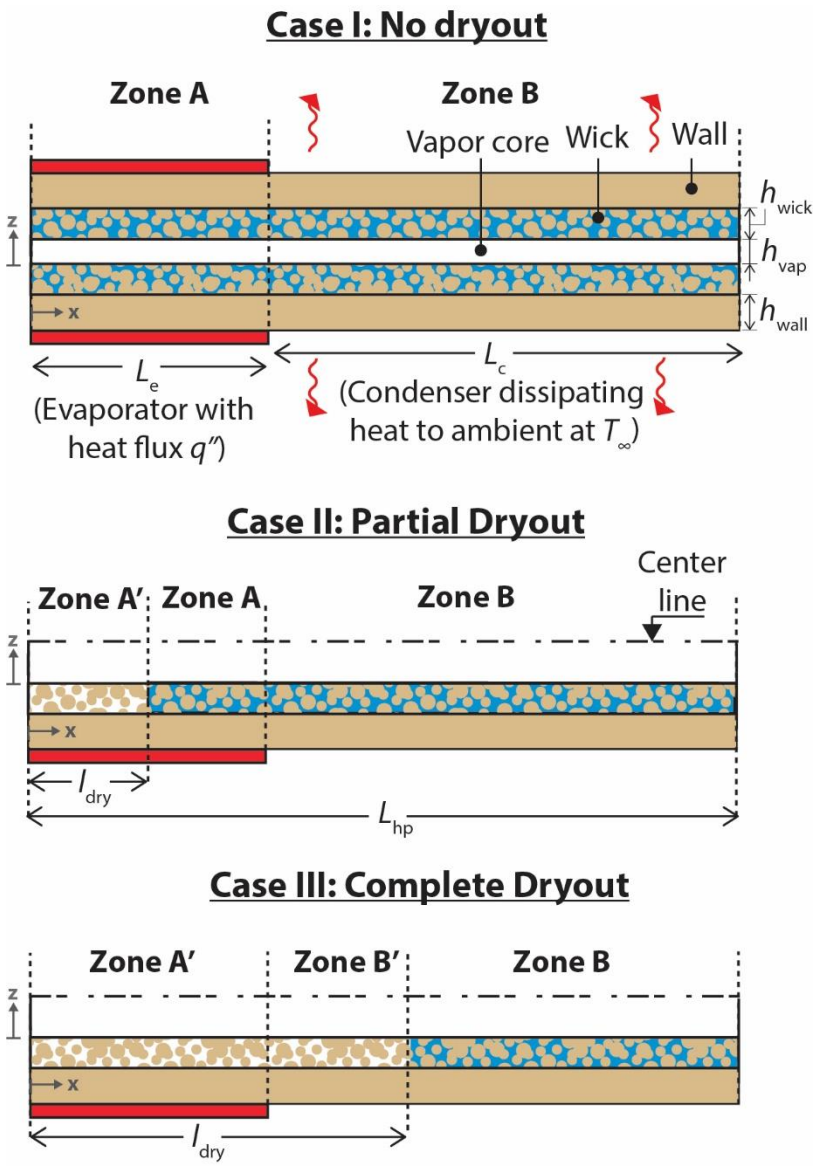

Figure 3. Model setup showing the liquid saturation along the wick in the heat pipe for three cases. The heat pipe has the evaporator section on the left end, while the remaining surface acts as the condenser. Case I has a liquid saturated wick, no dryout. Case II (only half geometry shown) is for partial dryout where the wick has a dry patch extending over a portion of the evaporator region. Case III is for complete dryout where the dry patch covers the entirety of the evaporator. In all three cases, the heat pipe is divided into zones for modeling purposes, where Zone A is the saturated evaporator and Zone B is the saturated condenser, Zone A′ is the dry evaporator region and Zone B′ is the dry condenser region.

4.1 Thermal model for the wall and the wick

A control-volume analysis is performed for energy transfer within each zone (A, A′, B, B′) in all the cases. The effective thermal conductivity of the wick is much smaller compared to that of the heat pipe wall and the vapor core [10]. This assumption is based on the several experimental works (as reviewed by Bodla et al. [30]) and the seminal theoretical work of Carson et al. [31], which have concluded that the effective thermal conductivity of the heat pipe wicks for the porosity range observed in commercial heat pipes is much less than that of solid copper which is the wall material. Hence, it is assumed that the thermal resistance to axial conduction through the wick is relatively large compared to other axial heat transfer pathways through the wall and vapor core. Moreover, for the range of extremely small heat pipe thickness used in current work (0.62 mm to 2 mm), the normal wick thermal resistance is relatively small compared to the heat transfer resistance through the vapor core and hence neglected in the analysis [12]. Furthermore, convective heat transfer in the wick is neglected since the diffusive transport dominates the advective energy transport [32]. The temperature drop across the wall thickness in the *z* direction (Figure 3) is also neglected.

For Zone A which represents the liquid-saturated evaporator (in Case I), the energy balance is performed between the external heat input, conductive heat transfer in the wall, and evaporative heat transfer from the wick, resulting in

$$\frac{\partial^2 T_{\mathrm{A}}}{\partial x^2} + \frac{q''}{k h_{\mathrm{wall}}} - \left(\frac{\phi h_{\mathrm{fg}}}{k h_{\mathrm{wall}}} \left(T_{\mathrm{A}} - T_{\mathrm{sat}} \right) \right) = 0 \qquad (1)$$

$$\text{where } \phi = \frac{2\sigma}{2-\sigma} \frac{h_{\mathrm{fg}} \rho_v}{T_{\mathrm{sat}}^{1.5}} \left(\frac{1}{2\pi R_{\mathrm{g}}} \right)^{0.5}$$

where the second term in the above equation account for the energy addition due to external heat input, and the third term accounts for evaporative heat transfer from the control volume. Note that the wall temperature for Zone A (T_{A}) is dictated by the vapor core saturation temperature (T_{sat}) which is computed during the model solution.

For Zone A′ (in Case II and Case III), no evaporation can occur in the dried-out evaporator region, and so the governing equation for wall temperature ($T_{\mathrm{A}'}$) is a result of conservation between external heat input and conductive heat transfer:

$$\frac{\partial^2 T_{A'}}{\partial x^2} + \frac{q''}{k h_{wall}} = 0 \tag{2}$$

For the saturated condenser region Zone B (in Case I, Case II and Case III), the energy balance is between the convective heat dissipation to ambient, evaporation/condensation heat transfer from the wick, and conductive heat transfer in the wall:

$$\frac{\partial^2 T_B}{\partial x^2} - \left(\frac{h}{k h_{wall}} \left(T_B - T_\infty \right) \right) - \left(\frac{\phi h_{fg}}{k h_{wall}} \left(T_B - T_{sat} \right) \right) = 0 \tag{3}$$

where T_B is the wall temperature for Zone B and h is the convective heat transfer coefficient to the ambient.

For the dried-out condenser region Zone B′ (in Case III), the energy balance is between convective heat transfer to the ambient and conductive heat transfer in the wall:

$$\frac{\partial^2 T_{B'}}{\partial x^2} - \frac{h}{k h_{wall}} \left(T_{B'} - T_\infty \right) = 0 \tag{4}$$

In each case, the governing equations for the zones are coupled using the boundary conditions of flux and temperature continuity at the boundaries between zones and adiabatic conditions at the zone boundaries at the ends of the heat pipe.

4. 2 Vapor core hydrodynamics

Vapor transport is assumed to be 1-D incompressible, quasi-steady, and diffusive. The vapor core control volume analysis is identical for both Zone A and Zone B. For Zone A′ and B′, the vapor core saturation pressure is assumed to be spatially uniform.

The pressure drop in the vapor core is assumed to be uniform along the normal direction (z) and thus can be expressed as:

$$\frac{1}{\mu_v} \frac{\partial P_v}{\partial x} = \frac{\partial^2 u_v}{\partial z^2} \tag{5}$$

where P_v is the pressure in the vapor core and u_v is the vapor core velocity along the *x*-direction. Using a no-slip boundary condition for the vapor flow in the vapor core, equation (5) can be integrated to give

$$u_v = \frac{1}{2\mu_v}\frac{\partial P_v}{\partial x}\left(z^2 - z h_{\text{vap}}\right) \tag{6}$$

Equation (6) is averaged along the vapor core thickness to obtain *z*-averaged vapor velocity. Performing a mass balance over an elemental control volume in the vapor core, and substituting in the *z*-averaged vapor velocity results in

$$\frac{\partial^2 \bar{P}_v}{\partial x^2} = \frac{-12\mu_v}{\rho_v h_{\text{vap}}^3}\left(m''_{\text{evap}} + m''_{\text{cond}}\right) \tag{7}$$

where $\bar{P}_v$ is the vapor core pressure averaged along the vapor core thickness. The pressure in the vapor core thus can be related to the saturation temperature using a linearized version of the Clausius-Clapeyron equation, resulting in

$$k_v \frac{\partial^2 T_{\text{sat}}}{\partial x^2} - \frac{\phi h_{\text{fg}}}{h_{\text{wall}}}\left(T_{\text{sat}} - T_{\text{A or B}}\right) = 0 \tag{8}$$

$$\text{where } k_v = \frac{\rho_v h_{\text{vap}}^3 h_{\text{fg}}^2 P_{\text{o,sat}}}{24\mu_v R_{\text{g}} T_{\text{o,sat}}^2 h_{\text{wall}}}$$

The boundary conditions for solving this equation assume zero saturation temperature gradient at $x = L_e - l_{\text{dry}}$ and $x = L_{\text{hp}}$.

4.3 Wick hydrodynamics

For momentum transfer in the wick (in Zone A and Zone B), it is assumed that the flow of liquid is incompressible and follows Darcy's law. The pressure drop in the wick thus can be written as

$$\frac{dP_{\text{wick}}}{dx} = -\frac{\mu_l}{K} u_l(x) \tag{9}$$

Here, $u_l(x)$ is the flow velocity that varies spatially due to local evaporation and condensation from the wick, and can be expressed as

$$u_l(x) = \frac{-1}{\rho_l h_{\text{wick}}} \int_{\substack{\text{saturated} \\ \text{length}}} \phi\left(T_{\text{A or B}} - T_{\text{sat}}\right)\, dx \tag{10}$$

As the spatial temperature distribution is first calculated from the thermal model and vapor core hydrodynamic model, equation (9) and equation (10) can be integrated numerically to find the total pressure drop in the wick. The wick-liquid-vapor contact angle can thus be computed as

$$\cos\theta = \frac{\Delta P_{\text{wick}}}{P_{\text{c,max}}} \tag{11}$$

Here, $P_{\text{c,max}}$ is the maximum capillary pressure that the wick can provide. It should be noted that for the heat pipe cases modeled and characterized in the current work, the pressure drop across the vapor core is negligible compared to the pressure drop in the wick [12]. Hence, ΔP_{wick} approximates the total pressure drop in the heat pipe.

4.4 Solution approach

Equations (1)-(4), (8) and (9) form a complete set of ordinary differential equations that can be solved analytically. In the model solution approach, the equilibrium position of the interface in the wick is governed by the stage of operation (powering-up or powering-down), such that the calculated interface position satisfies mass, momentum, and energy transfer in the heat pipe. During the powering-up or powering-down stages, the contact angle is computed in a manner by which the pressure drop in the wick at a given input power is balanced by the capillary pressure that the wick provides. The interface is allowed to recede if the contact angle θ (computed in equation (11)) reaches the receding contact angle, while the interface advances if the contact angle reaches the advancing contact angle. It directly follows from the solution procedure that the interface position remains unchanged if the contact angle is between the advancing and the receding contact angles. Correspondingly, a range of power inputs will exist for a given equilibrium interface position where the pressure drop in the heat pipe is balanced by the wick capillary pressure head.

5. Verification of the thermal hysteresis mechanism

The primary purpose in developing the model is to verify the proposed mechanism governing thermal hysteresis behavior during recovery from dryout in a heat pipe. However, predicting the thermal hysteresis during recovery from dryout requires various wick properties as inputs to the model, in particular the advancing and receding contact angles, which are typically unavailable or not known with confidence for commercial heat pipe samples. Therefore, best estimates of these properties, as listed in Table 1, are used as inputs to the model; we emphasize that the objective here is not a quantitative comparison with experiments, but rather to observe the thermal hysteresis behavior and assess whether the model captures

key experimental trends. Note that $P_{c,max}$ in equation (11) is calibrated such that the wick pressure drop at the capillary limit is balanced by $P_{c,max}$. To verify the proposed hysteresis mechanism, in the following subsections, parametric trends of the dryout recovery behavior are first generated using the model and then compared to experimental observations.

Table 1. Parameter inputs to the model for predicting post-dryout recovery.

Parameter	Value
Capillary limit	6.1 W
h	160 $Wm^{-2}K^{-1}$
h_{vap}	210 µm
h_{wall}	200 µm
h_{wick}	50 µm
K	1 x 10^{-11} m^2
L_e	10 mm
L_{hp}	130 mm
T_∞	25 °C
W	8.6 mm
Wick porosity	0.5
Working fluid	Water
θ_a [26]	66°
θ_r [26]	10°

5.1. Effect of extent of dryout on recovery behavior

Pulsing a heat pipe to higher heat loads above the capillary limit leads to a larger dryout region immediately after the pulse. This impact of a larger dryout region due to a higher pulse load on the powering-down curves is studied using both the model and experiments.

As noted in Section 4.4, due to the wetting hysteresis, a range of steady power inputs can exist where a given dryout length is in equilibrium. At this equilibrium, the heat pipe pressure drop is balanced by the capillary pressure head as the interface contact angle (equation (11)) adjusts between the advancing and the receding contact angles with changing power input. Hence, depending on the magnitude of the steady-state load following the pulse load, the dryout length may decrease if the contact angle is at the advancing angle ($\theta = \theta_a$) or remain unchanged ($\theta_r < \theta < \theta_a$). In the model, to capture the effect of increasing pulse magnitudes on the powering-down curves, the thermal resistance during recovery from dryout is computed at increasing

initial dryout lengths, where a higher initial dryout length serves as a proxy for a higher pulse load. Here, a parameter β is introduced for the extent of dryout, defined as the ratio of the initial dryout length to the total length of the heat pipe.

The following discussion briefly describes the process for obtaining a powering-down curve using the model. For a given magnitude of β and input power, the contact angle at $x = l_{dry}$ (that is $x = \beta * L_{hp}$) is evaluated and dryout length remains unchanged if the contact angle is between the receding and the advancing contact angle. However, if the contact angle is greater than the advancing contact angle, the dryout length is reduced such that the wick pressure drop is balanced by the capillary head at the advancing contact angle. The thermal resistance corresponding to the evaluated dryout length is computed, and the input power is then reduced to compute the dryout length (and thermal resistance) at the new input power. The process is repeated for decreasing input powers to obtain the powering-down curve for a given magnitude of β. A family of powering-down curves is thus generated for increasing magnitude of β. For obtaining the powering-up curve, the length of the dry patch is taken as zero ($\beta = 0$) for the range of input powers up to the capillary limit.

Figure 4 shows the predicted trend of normalized thermal resistance (normalized such that the values span between 0 and 1) with normalized power input (normalized with the capillary limit) for the powering-up curve ($\beta = 0$) and family of powering-down curves corresponding to each different initial value of β. The powering-down curves with higher thermal resistance correspond to higher β values (larger initial extent of dryout).

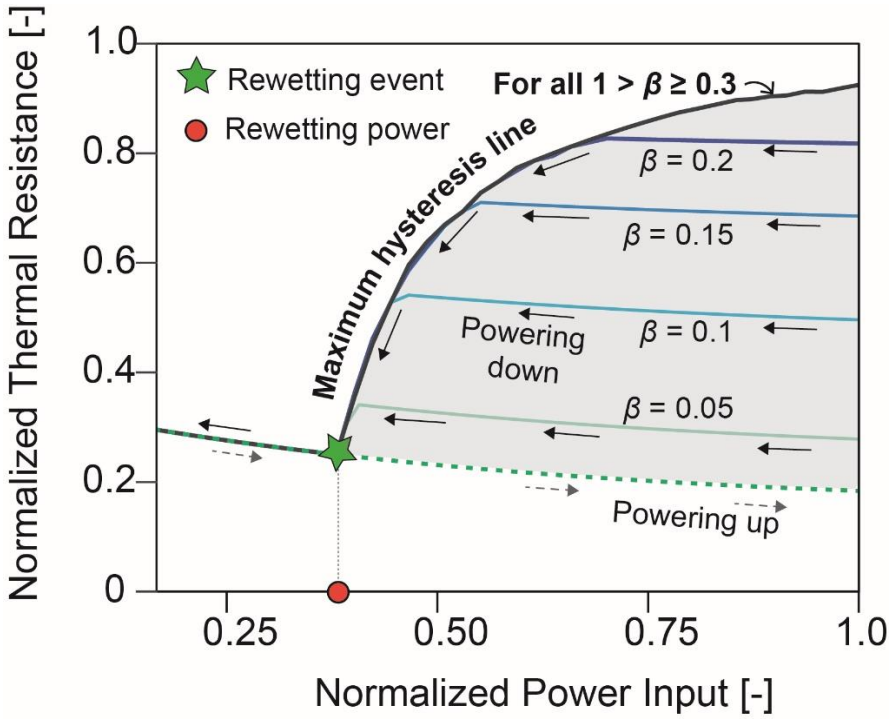

Figure 4. Predicted trend of post-dryout heat pipe recovery from increasing extents of dryout. A family of powering-down curves is shown corresponding to increasing extent of dryout (β) due to higher magnitudes of dryout-inducing pulse load. The power input and the thermal resistance magnitudes are normalized. All the powering-down curves decrease along a unique line, called the *maximum hysteresis line* (as marked in the figure). The powering-down curves merge with the powering-up curve at a unique heat input, termed the *rewetting power*.

The powering-down curves are characterized by a marginally changing thermal resistance as the power input is reduced from the dryout condition. This relatively flat thermal resistance is larger for higher initial extents of dryout. However, at some sufficiently low heat input, each powering-down curve begins to show a decrease in thermal resistance, and this input level matches the predicted power input from the model at which the interface has reached the advancing contact angle and the dryout patch begins to rewet. The key observation from these predictions is that all the powering-down curves decrease in thermal resistance along a single line, termed as the *maximum hysteresis line* as indicated in Figure 4. Therefore, all the possible powering-down curves for the heat pipe case considered here will exist in the region (shaded in gray) encompassed by the maximum hysteresis line. This maximum hysteresis line thus represents the worst-case

scenario (maximum thermal hysteresis) that can occur in a heat pipe during recovery from the most severe possible case of dryout. In Figure 4, the line corresponding to $\beta = 0.3$ is the maximum hysteresis line, and all the powering-down curves for any greater extents of dryout ($1 > \beta \geq 0.3$) overlap with each other. As the decrease in thermal resistance along the maximum hysteresis line is a result of wick rewetting, it follows that the contact angle of this advancing interface will be the advancing contact angle. Moreover, all the powering-down curves converge with the powering-up curve at a single power input. Termed as the *rewetting power*, this is the power below which the heat pipe must be operated to fully recover its performance after a dryout event, regardless of the extent of dryout. It should be noted that the rewetting heat input can be substantially lower than the capillary limit.

The characteristic behavior of heat pipe hysteresis and recovery from increasingly severe extents of dryout is now verified using experiments. Referring to Figure 1, the heat pipe used for the following experiments has a thickness (t_{hp}) of 0.87 mm, width (W) 8.6 mm and length (L_{hp}) 130 mm. Figure 5(a) shows a schematic power input profile that was applied to the heat pipe in these experiments. The heat pipe is pulsed from zero power to increasing magnitude heat inputs to create larger initial extents of dryout before performing the powering-down thermal resistance characterization procedure for each case. A steady-state powering-up curve is also acquired for reference. The powering-up and family of powering-down curves are shown in Figure 5(b), where the magnitude and duration of the initial power pulse is indicated by the legend. The data points are the experimental measurements, with thicker overlaid solid lines drawn to illustrate the inferred trend based on the understanding of the behavior gleaned from the model. The hysteresis and recovery behave exactly as suggested by the model. It is observed that different extents of dryout lead to different powering-down curves, and each powering-down curve has a range of near-constant thermal resistance followed by a decrease in thermal hysteresis relative to pre-dryout performance. The regions of decreasing thermal resistance all collapse along a single line, which is indeed the characteristic *maximum hysteresis line* identified by the model predictions in Figure 4. Lastly, all the powering-down curves merge with the powering-up curve at a single power input value of 2 W, which is the *rewetting heat input*. Given the complex nature of trends in the thermal resistance, this demonstration unequivocally verifies that the mechanism underlying the thermal hysteresis has been correctly identified as wetting hysteresis.

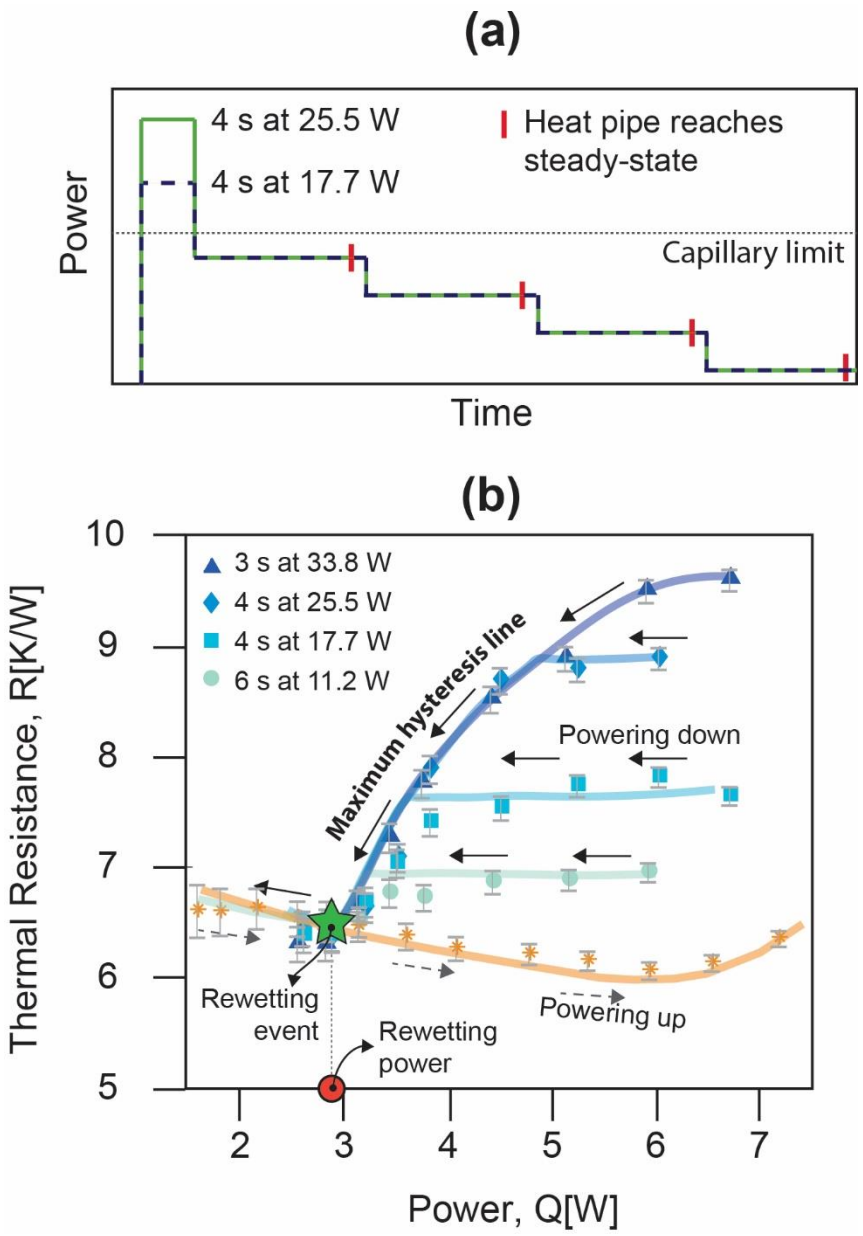

Figure 5. Experimentally observed trend of post-dryout recovery for increasing extents of dryout. (a) Representative power trace (shown only for two pulses with 4 s duration for illustration purposes) used to generate powering-down curves with an increasing extent of dryout. (b) Powering-up thermal resistance curve, with family of powering-down curves from increasing levels of dryout-inducing pulse loads.

While the maximum hysteresis line in Figure 5 is unique to the specific heat pipe sample and boundary conditions utilized during the experiments, the nature of recovery from dryout characterized by a maximum hysteresis line is observed in other heat pipe samples as well with different geometry and/or wick type.

Additional experimental results showing powering-up and powering-down curves for the two other heat pipe samples are shown in the Appendix A. One of the heat pipe samples has a circular cross section with 3 mm diameter, 250 mm length, and a sintered particle wick, while the other sample is a flat heat pipe with 130 mm length, 8.6 mm width, 0.62 mm thickness, and has a fiber wick. For both of these heat pipes (Figure A1 and Figure A2) undergoing recovery from dryout, the maximum hysteresis line is observed, asserting that maximum hysteresis line is present in heat pipes with different geometry and/or wick type. Appendix B further discusses a comparison between experimental data and the inferred trend from the model in the change in the maximum hysteresis line with changing adiabatic/condenser length and heat transfer coefficient to the ambient; the model captures the experimentally observed change in the maximum hysteresis line for changing adiabatic/condenser length and heat transfer coefficient to the ambient.

6. Novel test procedure for characterizing heat pipe recovery from dryout

All of the experimentally observed trends for the effects of the extent of dryout, change in adiabatic length, and change in condenser heat transfer coefficient on post-dryout recovery of the heat pipe follow the behaviors inferred from the model developed above. This clearly establishes that the mechanism for the thermal hysteresis observed following dryout is the wetting hysteresis at the liquid-vapor-wick interface in the heat pipe.

Identification of the maximum hysteresis line introduced in Section 5.1 provides an important signature of a given heat pipe that should be characterized for any device that is expected to undergo brief periods of dryout. Once characterized, this maximum hysteresis line provides a bound for the worst-case hysteresis that can occur after dryout in a heat pipe. The heat input at which the hysteresis vanishes due to rewetting of the wick (rewetting heat input) is also inherently known from characterizing the maximum hysteresis line. Owing to its practical significance, we offer a procedure for experimentally obtaining the maximum hysteresis line as follows:

1. From an unheated state, pulse the heat pipe to a heat input exceeding the capillary limit for sufficient time duration to induce dryout (longer than the time-to-dryout introduced in Ref. [24]). The capillary limit can be characterized in advance, as demonstrated in Figure 2.
2. Subsequent to imposition of the pulse load, lower the heat input to a value just below the capillary limit and measure the steady-state thermal resistance of the heat pipe. Continue lowering the heat input in small, finite decrements and measure the thermal resistance at each heat input.
3. For the rewetting to be occurring along the maximum hysteresis line, the thermal resistance should monotonically decrease with decrease in the heat input during this powering-down process. If the

thermal resistance does not decrease even at much lower heat input levels, but rather stays constant for a range of input power, this would imply that the pulse load magnitude and duration in step 1 was insufficient to cause dryout to the extent that achieved the maximum hysteresis. In this case, the procedure should be repeated with a higher pulse load or a pulse of a longer duration till the maximum hysteresis behavior is observed.

Conclusions

In this work, a mechanism is proposed for the observed post-dryout thermal hysteresis in a heat pipe, and it is subsequently confirmed via experiments. An analytical model is developed based on the proposed mechanism to study the trend of heat pipe recovery from dryout. The predicted trends from the model are then verified using experiments to confirm the mechanism. The following key conclusions are drawn:

- When a heat pipe is subjected to heat input exceeding its capillary limit, the dryout induced prevents thermal performance from returning to pre-dryout levels even after the heat input is reduced below the capillary limit. The severity of this thermal hysteresis increases with an increase in the dryout-inducing pulse input or its duration.
- Contact angle hysteresis at the wick-liquid-vapor interface in a heat pipe governs the post-dryout thermal hysteresis observed. In particular, the advancing contact angle governs the rewetting of the interface during recovery from dryout.
- A model developed based on this proposed mechanism predicts that there is a maximum level of thermal hysteresis that can occur after dryout; this *maximum hysteresis line* is a characteristic that is unique to a given heat pipe, and is independent of the pulse load magnitude and duration.
- The thermal hysteresis after dryout vanishes at a unique heat input, called the *rewetting heat input*, regardless of the extent of dryout and whether maximum hysteresis was attained. The magnitude of rewetting heat input is observed to be much lower than the capillary limit and suggests that the heat input must be lowered significantly for the heat pipe to fully recover performance after dryout.
- Given the critical importance of the maximum hysteresis line and rewetting heat input to the post-dryout recovery of any heat pipe, a generalized experimental procedure is provided for characterization of these parameters.

Acknowledgement

Financial support for this work provided by members of the Cooling Technologies Research Center, a graduated National Science Foundation Industry/University Cooperative Research Center at Purdue University, is gratefully acknowledged. The heat pipes used for conducting experiments in this work were supplied by Novark Technologies.

Appendix A. Powering-up and powering-down curves for additional heat pipe devices

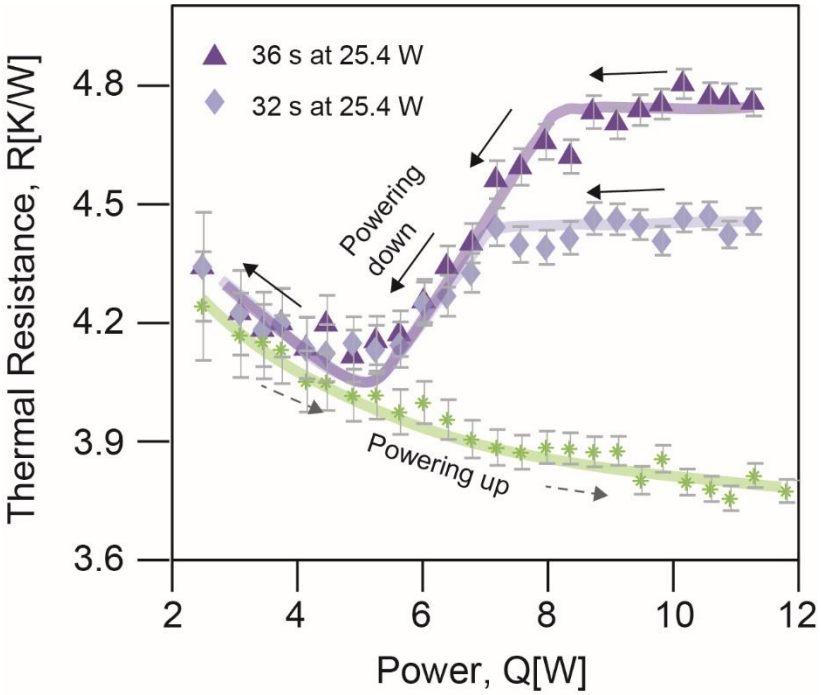

Figure A1. Powering-up and powering-down curves for a round heat pipe of 250 mm length and 3 mm diameter having a sintered wick. The powering-up (green) curve is obtained by increasing the heat input in finite increments from zero and measuring the heat pipe thermal resistance at each heat input. The powering-down curves are obtained as per the procedure mentioned in Section 5.1. The heat pipe is pulsed at 25 W for a brief time interval (two pulse durations indicated in the figure legend), after which the heat input is reduced to a value below the capillary limit.

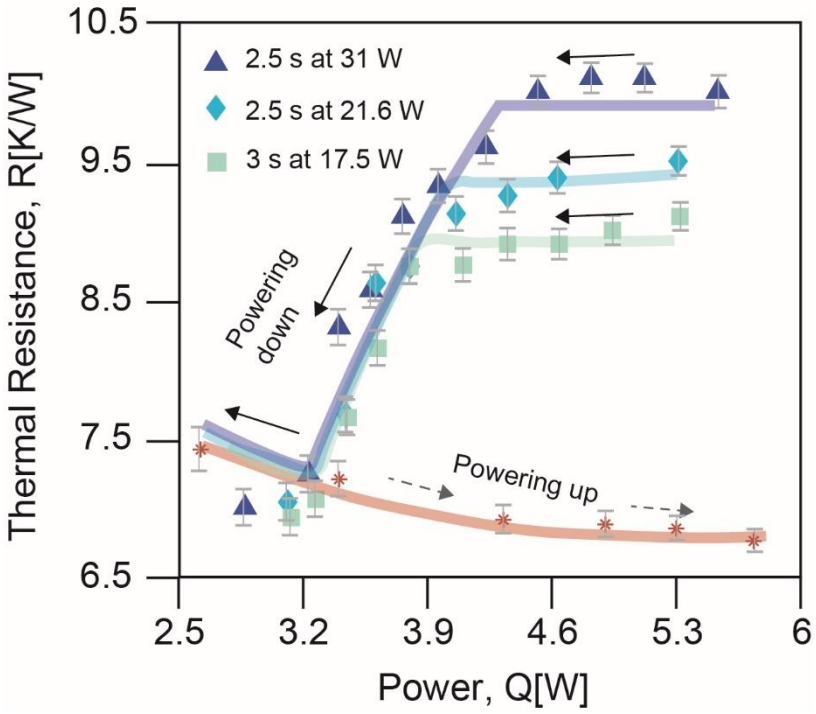

Figure A2. Powering-up and powering-down curves for a flat heat pipe of 130 mm length, 8.6 mm width, and 0.62 mm thickness, having a fiber wick. The time duration and pulse power input used to obtain the different powering-down curves are specified in the legend.

Appendix B. Effect of change in adiabatic/condenser length and heat transfer coefficient on maximum hysteresis line

B.1. Effect of adiabatic length on post-dryout recovery behavior

The wick pressure drop, and therefore the capillary limit of a heat pipe, scales with the effective flow length. For a heat pipe, the pressure drop in the wick is proportional to the effective fluid flow length in the wick, with the effective flow length typically defined as $(L_e + L_c + 2L_a)/2$, where L_e, L_c and L_a are shown in Figure 1 [3]. For a fixed heat pipe length, the effective flow length can be expressed simply as $(L_{hp} + L_a)/2$, where L_{hp} is the total length of the heat pipe (see Figure 1). Thus, a decrease in the adiabatic length while keeping the total heat pipe length fixed leads to a decrease in the wick pressure drop. For a given maximum capillary pressure head provided by the wick, a decrease in adiabatic length thus leads to an increase in the capillary limit and the rewetting heat input of the heat pipe.

For modulating the adiabatic/condenser length in the experiments, the convection shield (Figure 1) is adjusted along the heat pipe length so as to increase/decrease L_a. Note that during this process the total

length of the heat pipe does not change, hence an increase in adiabatic length would lead to a decrease in condenser length, while the evaporator length remains unchanged. Figure B1 shows the experimentally measured powering-up (star symbol) and powering-down (solid diamond) thermal resistance curves for two different adiabatic lengths. As in Figure 5, the solid lines are overlayed on the experimental data points in Figure B1 to illustrate the inferred trend based on the understanding developed from model predictions. The rewetting event during powering-down for both condenser lengths is marked by star symbol, and a vertical line on the *x*-axis from the rewetting event marks the rewetting power. As observed in Figure B1, the inferred trend from the model indicating a shift in the maximum hysteresis line with a decrease in adiabatic length is also observed in the experiments. The absolute magnitudes of thermal resistance during powering-up and powering-down also decrease as expected due to a decrease in adiabatic length given the larger condenser area available for heat removal to the ambient.

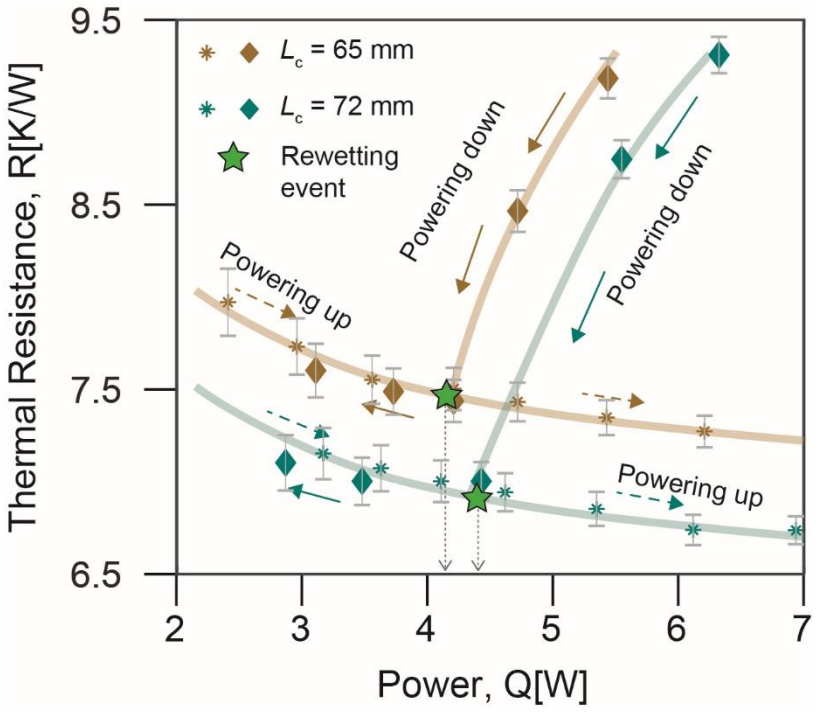

Figure B1. Powering-up (star symbol) and powering-down curves (diamond symbol) for two condenser lengths (L_c = 65 mm and 72 mm) for a heat pipe with length (L_{hp}) of 130 mm, width (W) of 8.6 mm and thickness (t_{hp}) of 0.87 mm. Solid symbols are experimental observations, while solid lines are drawn to depict the inferred trend from the model. The dashed arrows indicate the direction of powering-up, while the solid arrows indicate the direction of powering-down.

B.2. Effect of condenser heat transfer coefficient on recovery after dryout

The capillary limit of a heat pipe does not exhibit a strong dependence on the magnitude of condenser heat transfer coefficient to the ambient [34]. Since the wick pressure drop during recovery from dryout (powering-down) is related to maximum wick pressure head by a factor of $\cos(\theta_a)$ (see equation (11)), a change in condenser heat transfer coefficient to the ambient should not significantly affect the rewetting power of the heat pipe. To increase the heat transfer coefficient to the ambient in experiments (Figure 1), the volumetric air flow over the condenser surface is increased. Note that during this process, the total evaporator, adiabatic, and condenser lengths remain unchanged.

Figure B2 shows powering-up and powering-down curves for cases with two different heat transfer coefficients, with the solid lines representing the inferred trend from the model and the solid symbols are the experimentally observed data points. As in Figure B1, the rewetting event is marked by star symbol, and the vertical line on the *x*-axis from the rewetting event marks the rewetting power. As observed in the inferred trend from the model and in experiments, the rewetting power does remain practically unchanged with increase in heat transfer coefficient. A decrease in total thermal resistance is observed due to the decrease in the condenser-side thermal resistance at high heat transfer coefficients.

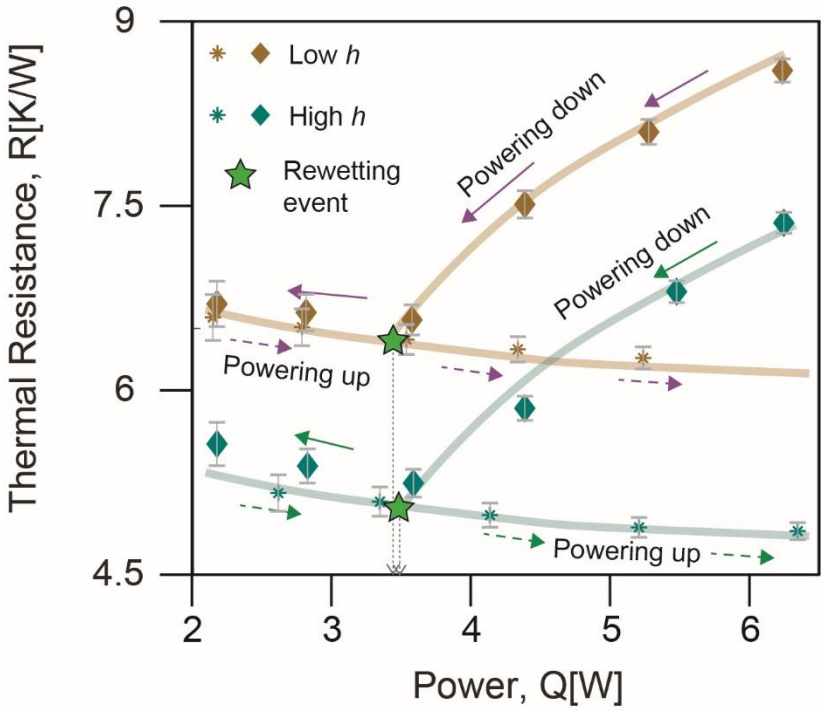

Figure B2. Powering-up (star symbol) and powering-down (diamond symbol) curves for demonstrating heat pipe recovery trend with change in heat transfer coefficient to the ambient. Solid symbols are the experimental data points, while solid lines are drawn to depict the inferred trend from the model. The heat pipe used here has a length (L_{hp}) of 130 mm, width (W) of 8.6 mm and thickness (t_{hp}) of 0.87 mm.

References

[1] R. Mahajan, C.P. Chiu, and G. Chrysler, "Cooling a Microprocessor Chip," *Proceedings of the IEEE*, vol. 94, 2006, pp. 1476–1486.

[2] A. Bar-Cohen and P. Wang, "Thermal Management of On-Chip Hot Spot," *ASME Journal of Heat Transfer*, vol. 134, 2012, pp. 553–567.

[3] S.W. Chi, *Heat pipe theory and practice: a sourcebook*, Hemisphere Publishing Corporation, Washington, DC, 1976.

[4] B.D. Iverson, T.W. Davis, S.V. Garimella, M.T. North, and S.S. Kang, "Heat and Mass Transport in Heat Pipe Wick Structures," *Journal of Thermophysics and Heat Transfer*, vol. 21, 2007, pp. 392–404.

[5] J.H. Liou, C.W. Chang, C. Chao, and S.C. Wong, "Visualization and Thermal Resistance

Measurement for the Sintered Mesh-wick Evaporator in Operating Flat-plate Heat Pipes," *International Journal of Heat and Mass Transfer*, vol. 53, 2010, pp. 1498–1506.

[6] S.C. Wong, J.H. Liou, and C.W. Chang, "Evaporation Resistance Measurement with Visualization for Sintered copper-powder Evaporator in Operating Flat-plate Heat Pipes," *International Journal of Heat and Mass Transfer*, vol. 53, 2010, pp. 3792–3798.

[7] S.C. Wong and Y.C. Lin, "Effect of Copper Surface Wettability on the Evaporation Performance: Tests in a Flat-plate Heat Pipe with Visualization," *International Journal of Heat and Mass Transfer*, vol. 54, 2011, pp. 3921–3926.

[8] R. Kempers, D. Ewing, and C.Y. Ching, "Effect of Number of Mesh Layers and Fluid Loading on the Performance of Screen Mesh Wicked Heat Pipes," *Applied Thermal Engineering*, vol. 26, 2006, pp. 589–595.

[9] J.Y. Chang, R.S. Prasher, S. Prstic, P. Cheng, and H.B. Ma, "Evaporative Thermal Performance of Vapor Chambers Under Nonuniform Heating Conditions," *Journal of Heat Transfer*, vol. 130, 2008, pp. 121501-.

[10] R.S. Prasher, "A Simplified Conduction Based Modeling Scheme for Design Sensitivity Study of Thermal Solution Utilizing Heat Pipe and Vapor Chamber Technology," *Journal of Electronic Packaging*, vol. 125, 2003, p. 378.

[11] I. Sauciuc, G. Chrysler, R. Mahajan, and R. Prasher, "Spreading in the Heat Sink Base: Phase Change Systems or Solid Metals??," *IEEE Transactions on Components and Packaging Technologies*, vol. 25, 2002, pp. 621–628.

[12] Y. Yadavalli, J.A. Weibel, and S.V. Garimella, "Performance-Governing Transport Mechanisms for Heat Pipes at Ultra-thin Form Factors," *IEEE Transactions on Components, Packaging and Manufacturing Technology*, vol. 5, 2015, pp. 1618–1627.

[13] K. Baraya, J.A. Weibel, and S.V. Garimella, "Simultaneous Wick and Fluid Selection for the Design of Minimized-Thermal-Resistance Vapor Chambers under Different Operating Conditions," *International Journal of Heat and Mass Transfer*, vol. 136, 2019, pp. 842–850.

[14] B.J. Jansen, A. Spink, and T. Saracevic, "Real Life, Real Users, and Real Needs: a Study and Analysis of User Queries on the Web," *Information Processing and Management*, vol. 36, 2000, pp. 207–227.

[15] M. Cha, P. Rodriguez, J. Crowcroft, S. Moon, and X. Amatriain, "Watching Television Over an IP

Network," *Proceedings of the 8th ACM SIGCOMM Conference on Internet Measurement*, New York, New York, USA: ACM, 2008, pp. 71–84.

[16] S.L. Jones, D. Ferreira, S. Hosio, J. Goncalves, and V. Kostakos, "Revisitation Analysis of Smartphone App Use," *Proceedings of the 2015 ACM International Joint Conference on Pervasive and Ubiquitous Computing*, New York, NY, USA: ACM, 2015, pp. 1197–1208, https://doi.org/10.1145/2750858.2807542.

[17] A. Visuri, Z. Sarsenbayeva, N. van Berkel, J. Goncalves, R. Rawassizadeh, V. Kostakos, and D. Ferreira, "Quantifying Sources and Types of Smartwatch Usage Sessions," *Proceedings of the 2017 CHI Conference on Human Factors in Computing Systems*, New York, NY, USA: ACM, 2017, pp. 3569–3581, https://doi.org/10.1145/3025453.3025817.

[18] J.M. Tournier and M.S. El-Genk, "A Heat Pipe Transient Analysis Model," *International Journal of Heat and Mass Transfer*, vol. 37, 1994, pp. 753–762.

[19] S. Harmand, R. Sonan, M. Fakès, and H. Hassan, "Transient Cooling of Electronic Components by Flat Heat Pipes," *Applied Thermal Engineering*, vol. 31, 2011, pp. 1877–1885.

[20] U. Vadakkan, S.V. Garimella, and J. Murthy, "Transport in Flat Heat Pipes at High Heat Fluxes From Multiple Discrete Sources," *ASME Journal Of Heat Transfer*, vol. 126, pp. 347–354.

[21] G. Patankar, J.A. Weibel, and S.V. Garimella, "On the Transient Thermal Response of Thin Vapor Chamber Heat Spreaders: Governing Mechanisms and Performance Relative to Metal Spreaders," *International Journal of Heat and Mass Transfer*, vol. 136, 2019, pp. 995–1005.

[22] E. Rotem, A. Naveh, D. Rajwan, A. Ananthakrishnan, and E. Weissmann, "Power-Management Architecture of the Intel Microarchitecture Code-Named Sandy Bridge," *IEEE Micro*, vol. 32, 2012, pp. 20–27.

[23] A. Shye, B. Scholbrock, and G. Memik, "Into the Wild : Studying Real User Activity Patterns to Guide Power Optimizations for Mobile Architectures Categories and Subject Descriptors," *Proceedings of the 42nd Annual IEEE*, 2009.

[24] K. Baraya, J.A. Weibel, and S.V. Garimella, "Heat Pipe Dryout and Temperature Hysteresis in Response to Transient Heat Pulses Exceeding the Capillary Limit," *International Journal of Heat and Mass Transfer*, vol. 148, 2020, p. 119135.

[25] F.A.L. Dullien, *Porous media : fluid transport and pore structure*, San Diego: Academic Press, 1992.

[26] T.P. Allred, J.A. Weibel, and S. V Garimella, “The Petal Effect of Parahydrophobic Surfaces offers Low Receding Contact Angles that Promote Effective Boiling,” *International Journal of Heat and Mass Transfer*, vol. 135, 2019, pp. 403–412.

[27] A. Horsthemke and J.J. Schröder, “The Wettability of Industrial Surfaces: Contact Angle Measurements and Thermodynamic Analysis,” *Chemical Engineering and Processing: Process Intensification*, vol. 19, 1985, pp. 277–285.

[28] K.T. Hong, H. Imadojemu, and R.L. Webb, “Effects of Oxidation and Surface Roughness on Contact Angle,” *Experimental Thermal and Fluid Science*, vol. 8, 1994, pp. 279–285, https://www.sciencedirect.com/science/article/pii/0894177794900582.

[29] D. Bonn, J. Eggers, J. Indekeu, J. Meunier, and E. Rolley, “Wetting and Spreading,” *Reviews of Modern Physics*, vol. 81, 2009, pp. 739–805.

[30] K.K. Bodla, J.Y. Murthy, and S. V Garimella, “Direct Simulation of Thermal Transport Through Sintered Wick Microstructures,” *Journal of heat transfer*, vol. 134, 2012, p. 012602.

[31] J.K. Carson, S.J. Lovatt, D.J. Tanner, and A.C. Cleland, “Thermal Conductivity Bounds for Isotropic, Porous Materials,” *International Journal of Heat and Mass Transfer*, vol. 48, 2005, pp. 2150–2158.

[32] G. Patankar, J.A. Weibel, and S.V. Garimella, “A Validated Time-stepping Analytical Model for 3D Transient Vapor Chamber Transport,” *International Journal of Heat and Mass Transfer*, vol. 119, 2018, pp. 867–879.

[33] R. Ranjan, J.Y. Murthy, S.V. Garimella, and U. Vadakkan, “A Numerical Model for Transport in Flat Heat Pipes Considering Wick Microstructure Effects,” *International Journal of Heat and Mass Transfer*, vol. 54, 2011, pp. 153–168.

[34] M. Aghvami and A. Faghri, “Analysis of Flat Heat pipes with various heating and cooling configurations,” *Applied Thermal Engineering*, vol. 31, 2011, pp. 2645–2655.